

Volumetric Acoustic Vector Intensity Probe

Earl G. Williams and Nicolas Valdivia

*Acoustics Division, Naval Research Laboratory, Washington D.C. 20375.**

Jacob Klos

NASA Langley Research Center, Hampton VA 23681

(Dated: February 6, 2006)

A new measurement tool capable of imaging the acoustic intensity vector throughout a large volume is discussed. This tool consists of an array of fifty microphones that form a spherical surface of radius 0.2m. A simultaneous measurement of the pressure field across all the microphones provides time-domain near-field holograms. Near-field acoustical holography is used to convert the measured pressure into a volumetric vector intensity field as a function of frequency on a grid of points ranging from the center of the spherical surface to a radius of 0.4m. The volumetric intensity is displayed on three-dimensional plots that are used to locate noise sources outside the volume. There is no restriction on the type of noise source that can be studied. The sphere is mobile and can be moved from location to location to hunt for unidentified noise sources. An experiment inside a Boeing 757 aircraft in flight successfully tested the ability of the array to locate flow-noise-excited sources on the fuselage. Reference transducers located on suspected noise source locations can also be used to increase the ability of this device to separate and identify multiple noise sources at a given frequency by using the theory of partial field decomposition. The frequency range of operation is 0 to 1400Hz. This device is ideal for the study of noise sources in commercial and military transportation vehicles in air, on land and underwater.

PACS numbers: 43.20.Ye, 43.40.At, 43.60.Pt, 43.60.Sx

I. INTRODUCTION

The measurement of acoustic intensity has long tempted the acoustician with its promises of localization and quantification of unknown noise sources and the determination of the sound power radiated from a machine.^{1,2} The acoustic intensity probe using two microphones is now a main stay of many measurements in industry and government. More sophisticated probes are appearing such as the three-axis intensity probe that provides the intensity vector at a point.³

Spherical arrays of microphones/hydrophones, that are the footing of this paper, have long been used in acoustics. Spherical harmonic decompositions of the measured field almost always form the basis behind the theory in these array systems and two early implementations were significant in acoustics.^{4,5} A very recent paper is a very good source of information about sound-field analysis using spherical arrays.⁶ Radar antenna measurements using spherical arrays has a rich history, much relying on spherical harmonic decompositions.^{7,8} Almost all of the research and development has been aimed at predicting the far-field from a knowledge of the near-field representing mathematically a well posed forward problem. The research introduced here we believe presents for the first time a volumetric and holographic projection of the intensity vector encompassing the volume in

the interior of a spherical array of microphones (well posed forward problem) as well as the volume just outside the sphere (ill-posed inverse problem). However, unlike the popular single axis and multiple axis vector intensity probes that provide high measurement accuracy our approach aims at more qualitative results, sacrificing high accuracy to image the intensity vector field at hundreds of points throughout a sizable volume, instantaneously. Furthermore this device is unique in its ability to isolate individual noise sources and map their intensity fields by using state-of-the-art signal processing.

We present in Sec. II a brief overview of basic theory of operation and design and in Sec. III we provide analytic formulas for the reconstruction error of the pressure field based on a plane wave source. A numerical experiment with a point monopole source outside the volume is presented in Sec. IV to articulate the errors of the intensity vector reconstructions. The front end signal processing used to isolate individual noise sources is described in Sec. V and application to an inflight experiment inside a Boeing 757 aircraft is presented in Sec. VI.

II. RECONSTRUCTION EQUATIONS

A hallmark of nearfield acoustical holography (NAH) is the reconstruction of the acoustic field in a volume, which we call a “volumetric reconstruction”, from information obtained on a surface. Spherical NAH provides the most ideal formulation for volumetric reconstructions, both in simplicity of theory and ease of application. Consider a

*Electronic address: williams@pa.nrl.navy.mil

spherical reconstruction volume \mathcal{V} represented by spherical coordinates $\mathbf{r} = (r, \theta, \phi) \in \mathcal{V}$ of extent defined by $0 \leq r \leq r_{max}$ which is source free (homogeneous wave equation applies) except for a "transparent" array of microphones located at $r = a < r_{max}$. The acoustic pressure, $p_\infty(\mathbf{r}, \omega)$, may be represented anywhere in \mathcal{V} by an expansion in terms of orthogonal spherical harmonics $Y_n^m(\theta, \phi)$ and spherical Bessel functions⁹ j_n :

$$p_\infty(\mathbf{r}, \omega) = \lim_{N \rightarrow \infty} p_N(\mathbf{r}, \omega),$$

where

$$p_N \equiv \sum_{n=0}^N \frac{j_n(kr)}{j_n(ka)} \sum_{m=-n}^n P_{mn}(a, \omega) Y_n^m(\theta, \phi), \quad (1)$$

with $k = \omega/c$ and a , the radius of the measurement surface. The unknowns P_{mn} in this equation are called the Fourier coefficients. The components of the velocity vector components are given in terms of these unknown Fourier coefficients⁹:

$$\begin{aligned} v_\theta(\mathbf{r}, \omega) &= \frac{1}{i\omega\rho} \sum_{n=0}^N \frac{j_n(kr)}{rj_n(ka)} \sum_{m=-n}^n P_{mn} \frac{\partial Y_n^m(\theta, \phi)}{\partial \theta} \\ v_\phi(\mathbf{r}, \omega) &= \frac{1}{i\omega\rho} \sum_{n=0}^N \frac{j_n(kr)}{rj_n(ka)} \sum_{m=-n}^n P_{mn} \frac{imY_n^m(\theta, \phi)}{\sin \theta} \\ v_R(\mathbf{r}, \omega) &= \frac{1}{i\rho c} \sum_{n=0}^N \frac{j_n'(kr)}{j_n(ka)} \sum_{m=-n}^n P_{mn} Y_n^m(\theta, \phi), \end{aligned} \quad (2)$$

where the equalities hold strictly only in the limit as $N \rightarrow \infty$. Note that these expressions use only j_n which is finite at the origin, as opposed to $h_n(kr)$ that is used when an array completely surrounds the sources of interest.^{4,5} Finally, the active intensity vector \vec{I} in spherical coordinates is then determined by the usual expression using unit vectors \hat{e} :

$$\vec{I}(\mathbf{r}, \omega) = \frac{1}{2} \Re[p_\infty^*(v_\theta \hat{e}_\theta + v_\phi \hat{e}_\phi + v_R \hat{e}_R)]. \quad (3)$$

For the VAIP the intensity is computed on a cubic lattice of points in \mathcal{V} and displayed in three-dimensional plots, as will be shown in Sec. IV.

The unknown Fourier coefficients $P_{mn}(a, \omega)$ are determined⁹ by integration over a sphere of the pressure field at $r = a$:

$$P_{mn}(a, \omega) \equiv \iint p_\infty(a, \theta, \phi, \omega) Y_n^m(\theta, \phi)^* d\Omega. \quad (4)$$

where $d\Omega \equiv \sin \theta d\theta d\phi$ and where p_∞ is derived from a temporal Fourier transform of the measured pressure in the usual way. The spherical array is designed so that the microphones are located at the quadrature points (θ_j, ϕ_j) , $j = 1, \dots, 50$, of an efficient algorithm to compute the surface integration in Eq. (4). One such efficient numerical quadrature algorithm is given by Lebedev^{10,11}

who provides a set of quadrature algorithms for optimum quadratures on a spherical surface for a range of microphone densities from 38 to 890. These algorithms are optimum by providing an exact integration of products of spherical harmonics up to a given sum of orders. The 50 element algorithm used in this paper integrates with no error products of spherical harmonics (say of order n' and n) up to $n + n' \leq 11$. Thus under this condition

$$\sum_{j=1}^{50} w_j Y_n^m(\theta_j, \phi_j) Y_{n'}^{m'}(\theta_j, \phi_j) = \delta_{mm'} \delta_{nn'},$$

where δ is the Kronecker delta and w_j are the quadrature weights. As we will see below this fact is critical. Even when $n = n' = 6$ most of the orthogonality still remains, so the quadrature algorithm breaks down "gracefully". Lebedev's algorithms are invariant with respect to octahedral symmetry, that is, the microphone locations on the spherical cap subtending one of the eight faces of the octahedron are identical (after rotation) on the other seven faces. Thus Eq. (4) is approximated by \hat{P}_{mn}

$$\hat{P}_{mn}(a, \omega) = \sum_{j=1}^{50} w_j p_\infty(a, \theta_j, \phi_j, \omega) Y_n^m(\theta_j, \phi_j)^*. \quad (5)$$

Since from Eq. (1)

$$p_\infty(a, \theta_j, \phi_j, \omega) = \sum_{n'=0}^{\infty} \sum_{m'=-n'}^n P_{m'n'} Y_{n'}^{m'}(\theta_j, \phi_j)$$

the algorithm forces

$$\hat{P}_{mn} = P_{m'n'} \delta_{mm'} \delta_{nn'} \quad \text{if } n + n' \leq 11. \quad (6)$$

Thus we are guaranteed that $\hat{P}_{mn} = P_{mn}$ as long as $n \leq 5$, i.e. the first 36 Fourier coefficients are determined without any integration error. For the computation of the pressure and velocity vector in Eqs. (1) and (2) we choose to use only these accurately computed Fourier and thus these sums are truncated to $N \leq 5$. We found that there was no gain in accuracy if we used the $n = 6$ Fourier coefficients.

The quadrature weights and locations in cartesian coordinates are easily derived using Lebedev's parameters listed under 11.1 in paper¹¹ and are not reproduced here for brevity.

III. ERROR ANALYSIS AND CONSIDERATION OF NOISE

One can derive analytical formulas of the error in the reconstruction of the pressure and velocity vector fields as a function of r if one assumes that the source is a plane wave and that the noise $\epsilon(\Omega)$ in the microphones is Gaussian and spatially incoherent with variance $\sigma^2 = E[|\epsilon|^2]$, where E is the ensemble average. The

derivation is presented in the reference⁹ for the normal velocity error, and the development for the pressure error is identical and thus is not presented here. We present results only for the pressure case, as the velocity cases present do not present any additional insight. Since these formulas are based on a plane wave source, they do not include the error due to presence of evanescent waves in the source field, waves that exist in the nearfield of sources. However, the formulas do provide valuable insight. It is assumed in this derivation that the Fourier coefficients are determined without error by the quadrature algorithm, as long as $N \leq 5$, as discussed above.

We define the root mean square error \mathcal{E} at a radius r using integration of the reconstructed field over a sphere of radius r (using Ω to represent (θ, ϕ)) as

$$\mathcal{E}(r) \equiv \left(\frac{\langle E[|p_\infty(r, \Omega) - p_N^\delta(r, \Omega)|^2] \rangle}{\langle |p_\infty(r, \Omega)|^2 \rangle} \right)^{1/2}, \quad (7)$$

where $\langle \bullet \rangle \equiv \frac{1}{4\pi} \iint \bullet d\Omega$. In this equation p_∞ is the exact pressure with no noise and $p_N^\delta(r, \Omega)$ is defined, following Eq. (1), as

$$p_N^\delta \equiv \sum_{n=0}^N \frac{j_n(kr)}{j_n(ka)} \sum_{m=-n}^n \hat{P}_{mn}^\delta Y_n^m(\Omega), \quad (8)$$

constructed from the measured Fourier coefficients \hat{P}_{mn}^δ including noise, following Eq. (5):

$$\hat{P}_{mn}^\delta = \sum_{j=1}^{50} w_j p^\delta(a, \Omega_j) Y_n^m(\Omega_j)^*, \quad (9)$$

where $p^\delta(a, \Omega_j) \equiv p_\infty(a, \Omega_j) + \epsilon(\Omega_j)$ is the pressure measured at the j 'th microphone location. Certainly as $\sigma \rightarrow 0$ $p_N^\delta \rightarrow p_N$.

Following Chapter 7 of the reference⁹ to evaluate Eq. (7) we find, given a plane wave incident *at any angle*, that the root mean square error at r is

$$\mathcal{E}(r) = \left(1 - \sum_{n=0}^N (2n+1) j_n(kr)^2 + \frac{\sigma^2}{16\pi \langle |p_\infty|^2 \rangle} \sum_{n=0}^N (2n+1) \left(\frac{j_n(kr)}{j_n(ka)} \right)^2 \right)^{1/2}, \quad (10)$$

where we call the first two terms the “base system error” and the last (3rd) term the “noise error”. In the derivation of Eq. (10) the 16π in the denominator results from an additional approximation given by $\sum_{i=1}^{50} w_i^2 |Y_n^m(\Omega_i)|^2 \approx 1/4$, not in the reference.⁹

We study Eq. (10) to understand the basic errors that arise in the reconstructions. Note that in the “base system error” term that $\sum_{n=0}^\infty (2n+1) j_n(kr)^2 = 1$, so that the “base system error” diminishes to zero as N increases. Since N is limited due to Eq. (6), the base system error

can only be reduced by increasing the number of microphones in the array. For example, based on Lebedev's formulas¹¹ we would need 86 microphones to get to $N = 7$ and 170 to get to $N = 10$. Note also the remarkable result that this error does not depend on the radius of the array; any size array will encounter the same “base system error” when reconstructing the field at a radius r . The upper frequency limit of the VAIP is determined by the base system error, as will show below.

The “noise error” term in Eq. (10) is inversely proportional to the signal-to-noise ratio (SNR) $\langle |p_\infty|^2 \rangle / \sigma^2$ and increases with r . What is not clear is the critical fact that the noise error can be reduced by decreasing the limit of the summation N at the low frequencies. This fact leads directly to a regularization filter in n which we discuss in the next section.

A. Regularization filter

Figure 1 is a plot of $\mathcal{E}(r)$ of Eq. (10) for an SNR of 30 dB and various cutoffs N . In the results below $a = 0.2\text{m}$ the radius of the VAIP array. The four curves corresponding to the legend represent the error when the reconstruction radius r is 0.4m and when N is limited to the values indicated in the legend. We can see that at the lowest frequencies $N = 2$ provides the least error up to 200Hz, switching to $N = 3$ then to $N = 4$ at 400Hz and finally to $N = 5$ at and above 600 Hz. The solid line labeled $r = 0.4\text{m}$ follows the values of N with the minimum error. The variable cutoff in the n summation for minimum error in Eq. (10) represents a regularization filter (with no taper in n) that controls the $(kr)^n$ behavior of $j_n(kr)$ in its small argument domain, viz $kr < n$. Filters of this kind are critical to the success of NAH.¹²

Two solid lines below the $r = 0.4$ line in the figure represent the minimum error for two other reconstruction radii, $r = 0.3\text{m}$ and $r = 0.2\text{m}$ as labeled and show that the errors diminish significantly for smaller reconstruction radii. Although not shown the results at these two radii have the same transition frequencies as the $r = 0.4\text{m}$ case for minimum error, namely 200, 400 and 600 Hz corresponding with the same values of N . Thus, for example, $N = 2$ provides the smallest error in the range 0 to 200 Hz for all three radii.

Finally, the dashed line in fig. 1 labeled $r = 0.4\text{m}$, $\sigma = 0$ is a calculation from Eq. (10) of only the base system error at a reconstruction radius of 0.4m and $N = 5$. Since this curve follows the last legend curve (that includes noise) it is clear that the base system error dominates the high frequency regime (above 800 Hz in this figure). This fact sets the upper frequency limit of operation of the VAIP as well as the maximum reconstruction radius. Adding more sensors will decrease this error, as discussed above, and thus extend the high frequency limit of operation. Furthermore with respect to regularization, we note the important deduction that no regularization is needed above about 800 Hz since the noise error is

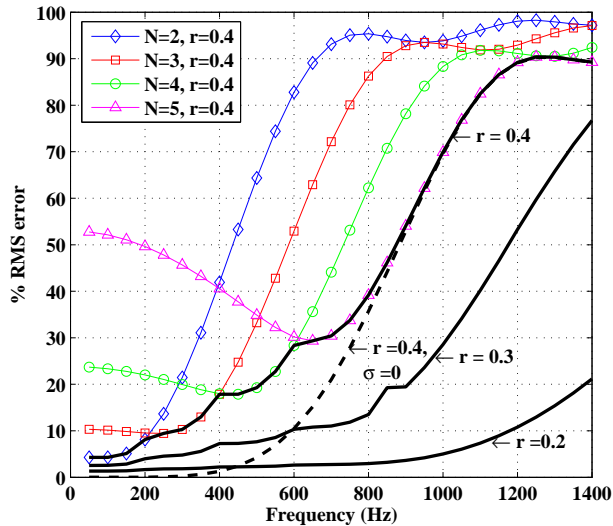


FIG. 1. Total error from Eq. (10) for 30dB SNR, $r = 0.4\text{m}$ and values of $N = 2, 3, 4, 5$. The solid curve labelled $r = 0.4\text{m}$ follows the values of N with the minimum error, and thus represents the actual error after regularization (choosing optimum value of N).

dominated by the base system error here. Contrarily, at the low frequencies the difference between the aforementioned two curves shows that the error is controlled by the noise error term of Eq. (10), not by the number of microphones in the array.

The simple regularization scheme presented above provides the potential to determine an a priori regularization scheme based on two variables, the frequency and the SNR as we will see in Sec. IV.A. We now turn to examine volumetric intensity reconstructions and the error associated with them.

IV. NUMERICAL EXPERIMENT WITH A POINT MONOPOLE SOURCE

We choose to model intensity errors using point sources instead of plane waves as was done above. The point source is an attempt to more correctly model the errors when the spherical array is placed close to vibrating surfaces. We choose a point source located outside the array in otherwise free space at distance of 1 meter from its origin. Its angular orientation with respect to the coordinate system of the array is irrelevant due to the important fact that *reconstructions are invariant to rotations of the spherical array*. This result follows from the faithful computation of the Fourier coefficients Eq. (9). One can not derive simple formulas, like those above for pressure reconstructions, to estimate the errors associated with reconstruction of the intensity vector field in the volume $r \leq 0.4\text{ m}$. Thus we resort to computer simulations in

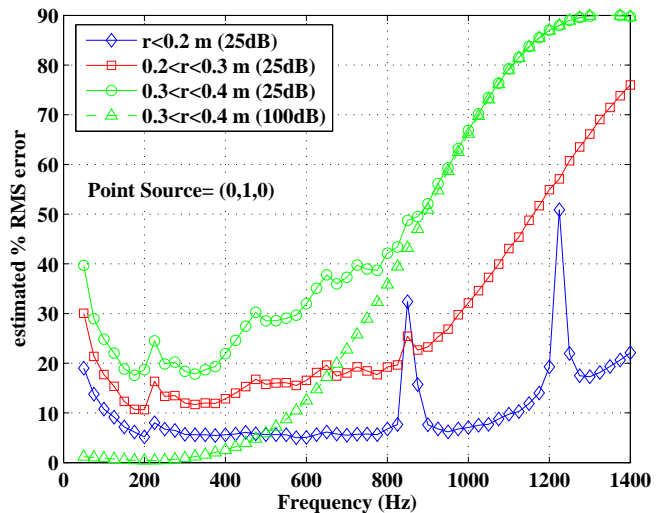


FIG. 2. Estimated root mean square intensity errors in different reconstruction volumes with added noise (SNR=25dB), for a point source at 1.0m from origin.

which the pressure field at each of the 50 microphones, to which is added a predetermined level of spatially uncorrelated random Gaussian noise, is computed. The exact intensity field without noise, computed at each of the reconstruction points in the volume, is known analytically since the point source is in a free field. This result is compared with the reconstruction of the vector field from the pressure hologram with added noise using Eqs. (1-4) (spherical NAH) and errors are determined. The level of random noise is set by the signal to noise ratio (SNR). The signal is defined as the RMS pressure level without noise “measured” by the 50 microphones and the noise is the square root of the variance of the added noise.

A. Estimated errors for intensity vector reconstruction

The reconstruction error for the intensity vector is defined by

$$\mathcal{E} = \frac{\|\vec{I}_{ex}(\mathbf{r}) - \vec{I}_{nah}(\mathbf{r})\|_2}{\|\vec{I}_{ex}(\mathbf{r})\|_2}, \quad (11)$$

where \vec{I}_{ex} is the exact intensity computed for a point source and \vec{I}_{nah} is the vector intensity reconstructed from the pressure with noise at the microphones and $\|\bullet\|_2$ is the L2 norm over a specified volume.

Figure 2 shows the results for the intensity error in three different reconstruction volumes defined by $r \leq 0.2$, $0.2 < r \leq 0.3$, and $0.3 < r \leq 0.4$, using an ensemble of numerical experiments with Gaussian noise added to the microphones with an SNR level of 25dB. The plots represent the minimum error determined by varying the values of N from 1 to 5; a manual regularization approach that

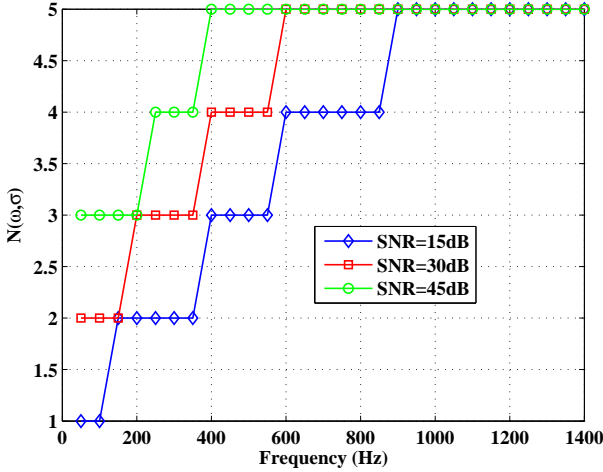


FIG. 3. Optimum regularization filter for a point source located 1m from the array center as a function of signal to noise ratio. The first three legend curves shown in fig. 2 used a regularization curve similar to the curve with the square symbols (30dB SNR).

determines the optimum filter. As with the pressure errors discussed above the error increases with reconstruction radius as well as with frequency. The fourth curve in the legend is for a 100dB SNR corresponding closely to a no noise case, for comparison to fig. 1. The two narrow peaks in the first legend curve arise from the zeros of $j_0(ka)$ and $j_1(ka)$ at 857 and 1225 Hz respectively that arise in the denominator of Eq. (1) and Eq. (2). To have a finite solution, the Fourier coefficients must be zero for $n = 0$ and $n = 1$ at these frequencies respectively. In other words the solution of the Helmholtz equation for the interior of a sphere is $j_n(kr)Y_n^m(\Omega)$ which exhibits a node at the problem frequencies. However, these Fourier coefficients are nonzero due to noise in the measurement, so the solution becomes infinite. This problem is eliminated by choosing an optimum filter that excludes the $n = 0$ term in a 10 Hz band about the 857 Hz zero, and the $n = 1$ term in a 10 Hz band centered at 1225 Hz. Although this filtering eliminates non evanescent fields and increases the error as the figure shows, a compromise must be struck to handle the indeterminacy of the reconstruction problem at the zeros of the denominator.

This optimum filter (minimum error) that was used to compute fig. 2 is shown in fig. 3 for three different values of signal to noise ratio (SNR). It is quite remarkable that the break points for the values of N for the 30dB curve are at 200, 400 and 600 Hz the same as determined for the plane wave source and the pressure reconstruction presented in fig. 1. This fact is important in justifying an a priori regularization filter that is fixed for the experiments discussed in Sec. (VI.A), a modification that speeds the processing of the VAIP and reflects our aim at real-time applications.

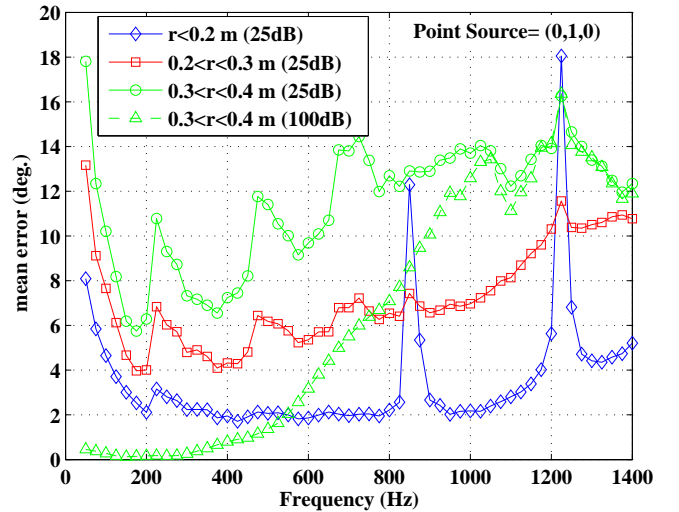


FIG. 4. Mean error in the angle of the reconstructed intensity vector for a point source at 1 m and an SNR 30dB. The error is calculated at three different reconstruction radii. The sudden jumps in the curves occur when the value of N changes.

Returning to fig. 2 it is clear that the intensity errors become very large in the outer reconstruction volume above 800 Hz. Although this might appear unacceptable (we will see below what the intensity field looks like with large error) it is important to consider a different view of the reconstruction accuracy, the error in the angle of the intensity vector. Errors in angle will be more misleading than amplitude errors as to the location of a concentrated noise source outside the array and conversely small angle errors will favor source ID even in the face of large magnitude errors. Figure 4 shows the mean of the error in the angle between the reconstructed intensity vector and the exact result for the same three reconstruction volumes presented in fig. 2. The error angle α between the reconstructed and the exact vector was computed using the dot product relation, $\cos(\alpha) = \vec{I}_{ex} \cdot \vec{I}_{nah} / (|\vec{I}_{ex}| |\vec{I}_{nah}|)$. Note that $\alpha \geq 0$. Comparisons were made only for intensity vectors of magnitude within 1/10 of the maximum magnitude as these are the vectors which are visible on a linear display. This figure shows the significant fact that the error in direction of the reconstructed intensity vectors in the volume is quite small.

B. Volumetric intensity reconstruction

Examples of the reconstructed intensity fields compared with the exact results for a point source located on the y -axis 1 meter from the origin are shown in the next set of figures, figs. 5-7 for three different frequencies. The SNR is 25dB and the intensity is plotted in the volume $r \leq 0.4$. In these figures the cones point to the direction of the intensity vector, and the length (and

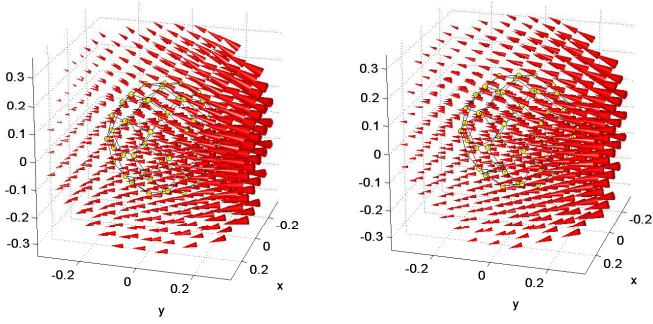


FIG. 5. Output from the VAIP at 250 Hz and 25dB SNR for a point source at 1.0m is shown on the left versus the exact field shown on the right both plotted on the same scale. The intensity vectors are plotted on a linear scale.

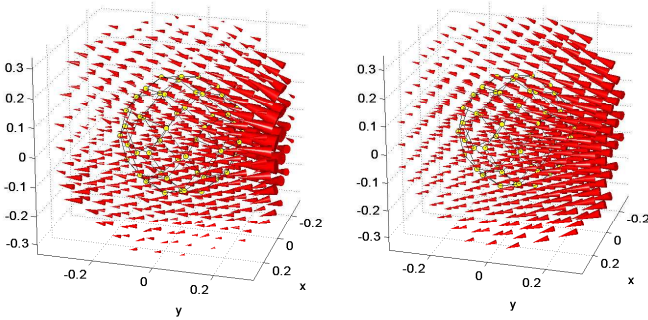


FIG. 6. Same as fig. 5 except at 800 Hz.

width) of the cone is proportional to the linear magnitude of the intensity. The center of the base of the cone is a point in a cubic lattice specifying the locations of the intensity vectors. The lattice spacing in each direction is 0.08 m. The 50 elements (small circles) of the measurement sphere are superimposed in each plot for reference. Results in figs 5-7 are for 250, 800 and 1150 Hz, respectively, with the exact result on the right and the reconstructed field on the left (plotted with the same

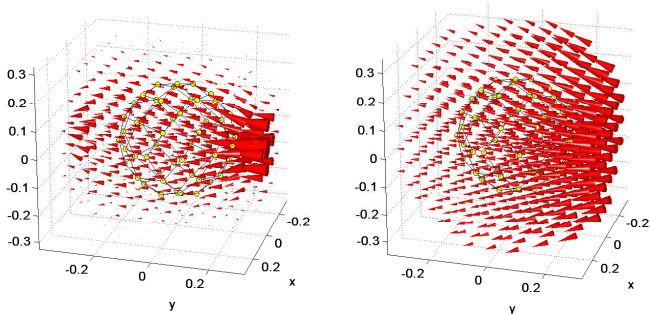


FIG. 7. Same as fig. 5 except at 1150 Hz.

scale). The essential conclusion drawn from these figures is that the direction of the point source (located on axis at $y=1.0$) is correctly indicated by the reconstructed field (left-hand plots) and the actual location can be found by the intersection of lines colinear with the intensity vectors near the source. In comparing to the exact result on the right panel of the figure note that accompanying errors in the three main reconstruction volumes $r \leq 0.2$, $0.2 < r \leq 0.3$ m and $0.3 < r \leq 0.4$ m, were given in fig. 2. The large errors in the outer volume $0.3 < r \leq 0.4$ m at the two higher frequencies are evident in the comparison if one concentrates on the vectors at the outer reaches of the volume in figs. 6 and 7. Note, however, the mean angle error of the visible vectors in this volume (according to 4) is less than 14 degrees at 800 Hz and 1150 Hz, so that even with the large amplitude errors and field distortion in the outer volume the direction and location of the point source is still determined. Again we want to emphasize that the errors at 800 and 1150 Hz arise from the base system error, and are not related to the SNR. To diminish these errors one must increase the number of microphones in the array so that more spherical harmonics are included as discussed in Sec. III.

The level of noise in these simulations was preset. However, it is generally not known during physical experiments and can be determined by the following procedure.^{12,13} We assume that the level of the evanescent waves with $n = 6$ associated with the source has decayed beyond the noise level (spatially uncorrelated) at the microphones. This decay is given in the region $kr < n$ by $j_n(kr) \approx (kr)^n / (2n+1)!!$, a power-law decay towards the origin. Thus we compute the standard deviation of the noise σ using $\sigma \approx E[|\hat{P}_{mn}^\delta|] / \sqrt{13}$ for $n = 6$ and a norm of the thirteen harmonics $m = -6, -5, \dots, 6$. This method works faithfully for frequencies $kr_{max} < 6$ or $f < 819\text{Hz}$ for $r_{max} = 0.4$. Above 800 Hz knowledge of the noise level is unnecessary since the errors are dominated by base system error, as discussed above.

The signals used in the simulations above were simple deterministic pressure fields measured at the microphone locations. However, in practice stochastic signals must be considered so that the VAIP can be used in field experiments with complex noise sources. We deal with these complex signals in the “front end” signal processing. This front end provides for the construction of partial field holograms using theory that has been developed over the past 15 years.

V. FRONT END SIGNAL PROCESSING

We summarize the front end theory briefly here and the reader is directed to the references for further information.¹⁴⁻¹⁹ This theory is used to expand the modes of operation of the VAIP. Although the VAIP can reconstruct intensity fields *without* reference transducers, due to the instantaneous measurement of the pressure

data, and identify noise sources by display of the directional intensity vectors radiated from those sources, it is possible to further separate multiple noise sources by using partial field decomposition techniques described in the references. The partial field approach was developed by Hald¹⁴ and has since found a multitude of industrial applications through the use of the STSF (spatial transformation of sound fields) approach.

Assume M reference transducers recorded simultaneously and Fourier transformed to provide raw spectra represented by $\mathbf{X}(f) \equiv (X_1 X_2 \cdots X_M)^t$ (t is transpose) along with the 50 microphone raw spectra $\mathbf{P}(f) \equiv (P_1 P_2 \cdots P_{50})^t$ with accompanying noise $\mathbf{N}(f) \equiv (N_1 N_2 \cdots N_{50})^t$. The reference transducers are generally attached to candidate (source) machines that are assumed to be random with Gaussian statistics, although they are not necessarily incoherent to one another. A transfer function matrix $\mathbf{H}^{(50 \times M)}$ with elements H_{ij} relates the pressure at the i 'th microphone and the j 'th reference through $\mathbf{P} = \mathbf{H}\mathbf{X} + \mathbf{N}$.

The autospectral density of the i 'th microphone is given by an ensemble average E of the raw spectra (using a long time series broken into shorter segments that are Fourier transformed) of the measured pressure

$$S_{p_i p_i}(f) = E[P_i^*(f)P_i(f)] = \mathbf{H}_i^H \mathbf{S}_{\mathbf{xx}} \mathbf{H}_i + S_{n_i n_i}, \quad (12)$$

where \mathbf{H}_i is the i 'th row of \mathbf{H} , the H superscript represents conjugate transpose.

Partial field decomposition techniques all decompose the autospectral density function of a microphone using an inner product of a partial field column vector Ψ_i of length M , $\Psi_i = (\Psi_{1i} \Psi_{2i} \cdots \Psi_{Mi})^t$, that is, $S_{p_i p_i} = \Psi_i^H \Psi_i + S_{n_i n_i}$. This decomposition can be accomplished by taking the square root (assumed positive definite) of the reference cross-spectral density matrix $\mathbf{S}_{\mathbf{xx}} = \sqrt{\mathbf{S}_{\mathbf{xx}}}^H \sqrt{\mathbf{S}_{\mathbf{xx}}}$, where (using an outer product)

$$\mathbf{S}_{\mathbf{xx}} \equiv E[\mathbf{X}^* \mathbf{X}^t] = \begin{pmatrix} S_{x_1 x_1} & S_{x_1 x_2} & \cdots & S_{x_1 x_M} \\ S_{x_2 x_1} & S_{x_2 x_2} & \cdots & S_{x_2 x_M} \\ \vdots & \vdots & \ddots & \vdots \\ S_{x_3 x_1} & S_{x_3 x_2} & \cdots & S_{x_3 x_M} \end{pmatrix},$$

so that Eq. (12) becomes

$$S_{p_i p_i}(f) = (\sqrt{\mathbf{S}_{\mathbf{xx}}} \mathbf{H}_i)^H \sqrt{\mathbf{S}_{\mathbf{xx}}} \mathbf{H}_i + S_{n_i n_i}.$$

The partial field components of the i 'th microphone are $\Psi_i \equiv \sqrt{\mathbf{S}_{\mathbf{xx}}} \mathbf{H}_i$. A partial field matrix Ψ is formed from these using $\Psi = (\Psi_1 \Psi_2 \cdots \Psi_M)$. The rows of Ψ form M partial field holograms, each processed separately for reconstruction of M volumetric intensity fields.

There are two standard procedures for taking the square root of a matrix: (1) the Cholesky decomposition

$$\mathbf{S}_{\mathbf{xx}} = \mathbf{T}^H \mathbf{T} \quad (13)$$

where \mathbf{T} is upper triangular and (2) SVD (singular value decomposition)

$$\mathbf{S}_{\mathbf{xx}} = \mathbf{U} \mathbf{\Sigma} \mathbf{U}^H \equiv \mathbf{U} \mathbf{\Sigma}^{1/2} \mathbf{\Sigma}^{1/2} \mathbf{U}^H, \quad (14)$$

where \mathbf{U} is unitary and $\mathbf{\Sigma}$ is diagonal. It is important to note that in our research we found that the Cholesky method gave identical results to the signal conditioning approach provided in Bendat and Piersol²⁰ and in one of the references.²¹ A great deal of theory is provided in Bendat's book about the signal conditioning approach which can then be directly applied to understanding Cholesky decompositions. The SVD method is also called the principal component method in the literature.

Since the transfer functions \mathbf{H}_i are not of interest here they are eliminated by use of the cross-spectral density column vector between the microphone and the references:

$$\mathbf{S}_{\mathbf{x}p_i} \equiv E[\mathbf{X}^*(f)P_i(f)] = E[\mathbf{X}^* \mathbf{X}^t] \mathbf{H}_i = \mathbf{S}_{\mathbf{xx}} \mathbf{H}_i$$

(the i 'th column of the cross-spectral density matrix $\mathbf{S}_{\mathbf{x}p}$) leading to

$$\mathbf{H}_i = (\mathbf{S}_{\mathbf{xx}})^{-1} \mathbf{S}_{\mathbf{x}p_i}$$

Thus the two procedures yield method I, Cholesky,

$$\Psi_i = (\mathbf{T}^H)^{-1} \mathbf{S}_{\mathbf{x}p_i}, \quad (15)$$

and method II, Principal Components (SVD),

$$\Psi_i = \mathbf{\Sigma}^{-1/2} \mathbf{U}^H \mathbf{S}_{\mathbf{x}p_i}. \quad (16)$$

One characteristic of the Cholesky method, and not of the SVD approach, is that the partial fields are dependent upon the order of the columns and rows of $\mathbf{S}_{\mathbf{x}p}$.²⁰ Thus it is necessary to carry out some pre-analysis in the Cholesky approach to set up the order of the references, choosing the most significant reference at a particular frequency to form the first row. We determine significance by choosing references that have the largest coherence to the microphones, computing the average coherence $\overline{\gamma_{x_i p}^2}$ of the i 'th reference to the 50 microphones:

$$\overline{\gamma_{x_i p}^2} \equiv \frac{1}{50} \sum_{j=1}^{50} \gamma_{x_i p_j}^2, \quad (17)$$

where $\gamma_{x_i p_j}^2 \equiv |S_{x_i p_j}|^2 / (S_{x_i x_i} S_{p_j p_j})$ which allows us to rank the references, x_m, x_n, \cdots, x_k , with respect to average coherence for each frequency:

$$\overline{\gamma_{x_m p}^2} > \overline{\gamma_{x_n p}^2} > \cdots > \overline{\gamma_{x_k p}^2}. \quad (18)$$

Here x_m and x_n are the references with the first and second largest average coherence, respectively.

Given this ranking of references we reorder $\mathbf{S}_{\mathbf{xx}}$ and $\mathbf{S}_{\mathbf{x}p}$ (separate order for each frequency):

$$\mathbf{S}_{\mathbf{xx}} \equiv \begin{pmatrix} S_{x_m x_m} & S_{x_m x_n} & \cdots & S_{x_m x_k} \\ S_{x_n x_m} & S_{x_n x_n} & \cdots & S_{x_n x_k} \\ \vdots & \vdots & \ddots & \vdots \\ S_{x_k x_m} & S_{x_k x_n} & \cdots & S_{x_k x_k} \end{pmatrix}^{(M \times M)} \quad (19)$$

$$\mathbf{S}_{\mathbf{x}\mathbf{p}} \equiv \begin{pmatrix} S_{x_m p_1} & S_{x_m p_2} & \cdots & S_{x_m p_{50}} \\ S_{x_n p_1} & S_{x_n p_2} & \cdots & S_{x_n p_{50}} \\ \vdots & \vdots & \ddots & \vdots \\ S_{x_k p_1} & S_{x_k p_2} & \cdots & S_{x_k p_{50}} \end{pmatrix} \quad (20)$$

so that the full reconstruction equation becomes, for example for the Cholesky method,

$$\Psi = (\mathbf{T}^H)^{-1} \mathbf{S}_{\mathbf{x}\mathbf{p}}. \quad (21)$$

The rows of $\Psi^{(M \times 50)}$ form M separate holograms ranked in order of importance, each of which can be used to reconstruct the volumetric intensity at a given frequency by replacing $p_\infty(a, \Omega_j, \omega)$ in Eq. (4) with one of the rows and computing the intensity vector Eq. (3) on a cubic lattice, displaying the results as in Sec. (IV).

A. Figures of merit

Finally we consider three important measures that bracket the significance of the partial coherence method for any particular experiment. The first is called the partial (or virtual) coherence Γ_{ij}^2 and represents what fraction of the signal energy $S_{p_j p_j}$ of the j 'th microphone is taken up by the partial field related to the i 'th reference:

$$\Gamma_{ij}^2 \equiv \frac{|\Psi_{ij}|^2}{S_{p_j p_j}}. \quad (22)$$

This ratio must be less than or equal to one. A value of one indicates that the i 'th reference accounts for all of the measured signal and that all other references do not participate in the measured signal at the j 'th microphone (an unlikely occurrence). The average over all the microphones is:

$$\Gamma_i^2 \equiv \frac{1}{50} \sum_{j=1}^{50} \frac{|\Psi_{ij}|^2}{S_{p_j p_j}}, \quad (23)$$

so that Γ_i^2 represents the fraction of the signal energy to all the microphones in the array due to the i 'th reference. Note that $\Gamma_i^2 \leq 1$. The final figure of merit is the total fraction of all the signal energy received by the array that is represented by all the references used in the partial field decomposition:

$$\Gamma^2 \equiv \sum_{i=1}^M \Gamma_i^2. \quad (24)$$

For example, if this fraction Γ^2 is equal to 0.6 we know that 60% of the signal energy received by the microphones has been represented by the M partial field holograms. When this number is low we might conclude that the reference set was poorly chosen, and that the dominant acoustic sources have been overlooked in the experiment. We will show examples of these measures in the next section.

VI. EXPERIMENTAL APPLICATION

A 50 element spherical array was designed and constructed at the Naval Research Laboratory (NRL) and is shown in fig. 6 in our in air laboratory on the left and in flight on the right. The microphones were 1/8 inch diaphragm electrets and were amplitude calibrated at 248 Hz. The phase response was not calibrated, but the 50 microphones were preselected for uniformity, resulting in a total phase variation of ± 2 degrees at 500 Hz. A light metal frame held the microphones in their positions that were determined by the quadrature algorithm, described above. The tips of the microphones formed a spherical array of radius 0.2 m and the signal cables were run down the vertical support rod shown in the figure. One aim of the design was for acoustic transparency. Initial experiments on a loudspeaker source in NRL's in-air facility were successful, but are not reported on here for the sake of brevity.

The picture on the right in fig. 6 shows the array in the NASA Aries Boeing 757-200 airplane which is dedicated to flight test operations for the NASA Langley Research Center. The data set we report on here is a small subset of a much larger recent experiment using this aircraft.²² In this experiment most of the seats in the aircraft were removed as well as the trim panels and insulation in four adjacent window sections as shown on the right in the figure. Also shown, but not reported on here, is a conformal nearly planar array of microphones located between the spherical array and the fuselage panel. The aircraft was flown at a tightly controlled altitude of 30,000 ft and speed of 0.8 Mach. Most of the bare panels and windows were monitored with accelerometers (a total of 31) placed at their centers and extra microphones (a total of 8) were dispersed throughout the aircraft interior. All of these monitors served as possible references for the VAIP as well as monitors of the physics of the vibration/radiation mechanics. All of the transducer channels were sampled simultaneously at 12,000 samples per second and recorded digitally on tape for processing in the laboratory. To provide a known source in the cabin Jacob Klos at NASA²² created a point source using a long tube coupled to a loudspeaker as shown in fig. 9. The outlet of the tube was at the center of the window, a few centimeters from its surface. The loudspeaker (shown in the figure on the right) was driven by a pseudo-random signal. This provided a guaranteed incoherent source to compare with the flow noise excited panels also radiating into the interior, and thus is a test of the front-end signal processing that should be able to separate multiple incoherent sources. We will show below the first three partial field holograms (rows of Ψ) and volumetric intensity maps produced by our procedure at selected frequencies for this experiment. A second experiment was done with the point source turned off, and again partial field holograms and volumetric intensity maps were determined and compared with the first experiment. The objectives here were (1) to show that VAIP successfully identified

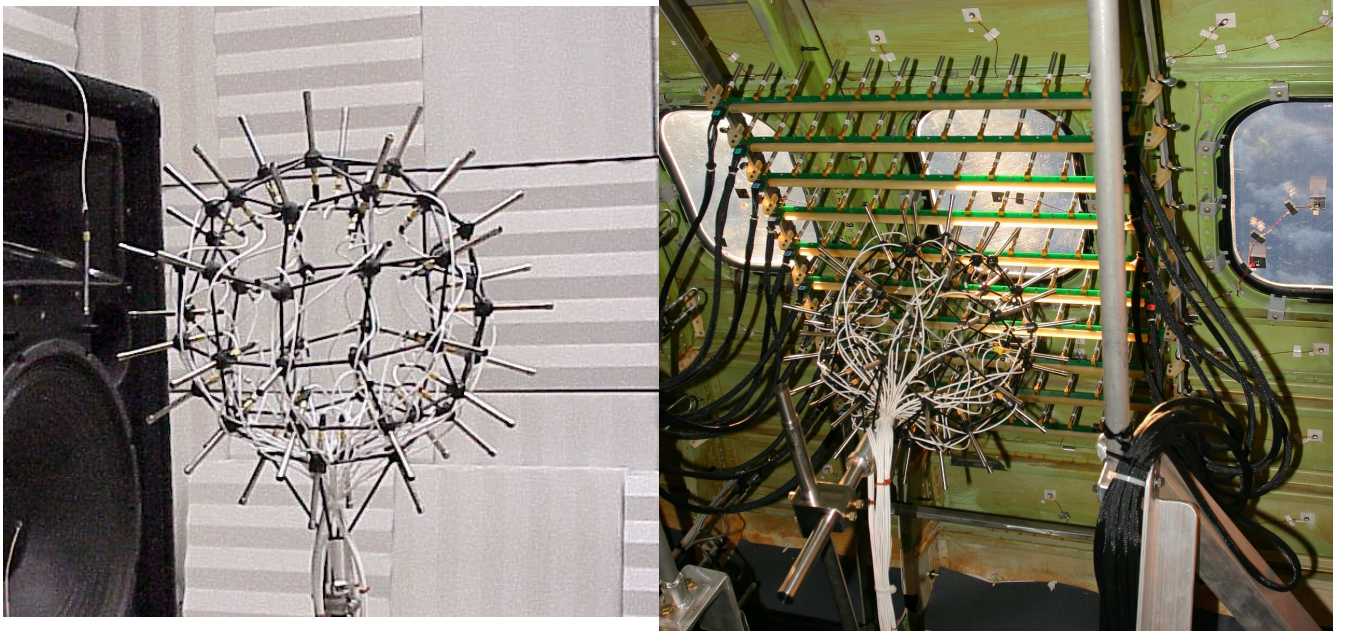


FIG. 8. NRL 50 element spherical array in NRL test facility (left) and in flight inside the 757 aircraft (right) shown behind a conformal array (not discussed in this paper) with horizontal beams of elements in front of a fuselage window.

the point source and the flow-noise induced panel source and (2) to show that the extraction of the flow-noise induced source was unique (unchanged with or without the point source).

A. Partial field holograms and intensity fields for point and flow noise sources

The 31 accelerometer references and the loudspeaker drive voltage (a pseudo-random band-pass signal between 500 and 1500 Hz) were all used as the reference set ($M=32$) to form the auto and cross-spectral density functions of Eq. (19) and Eq. (20). A set of ensembles (estimates of $X_m(f)$ and $P_i(f)$) was created consisted of 1200 non-overlapping segments of the time record, each containing 1920 points and Fourier transformed to provide frequency domain data. This was carried out for each microphone and each reference. Since the sample rate was 12kHz, the total record was 192 seconds. The average coherence Eq. (17) was then computed from these spectra and the references were ordered as to importance using Eq. (18). This was carried out at each frequency (6.25 Hz bins) in the band of interest (500-1400 Hz).

For brevity we present the results at a single frequency bin and note that the results are typical. The autospectral density of the accelerometer on the center of one of the panels below the window (dot marked number 17 in fig. 9) showed a maximum in response at 732 Hz indicating a resonance of the panel excited by flow noise. At this frequency the 1st three partial holograms (the three top rows of the matrix in Eq. (21)) were constructed us-

ing the Cholesky method from Eqs (20), (19), (13) and (21). Each of the partial holograms were then processed into volumetric intensity fields which we now describe.

Each partial field, a row of Eq. (21), replacing p_∞ in Eq. (5), is integrated by Lebedev quadrature to determine the Fourier coefficients. These coefficients \hat{P}_{mn}^δ determined up to $n \leq 5$ are used to compute the components of the pressure and vector intensity given by Eqs (1) and (2) leading to Eq. (3). Computations are repeated at a set of field points on a equal spaced cubic reconstruction grid with lattice size of 8 cm. This cartesian grid proved to be most effective at display of the intensity vector. The intensity computations are limited to within the sphere of radius 0.4m, due to the high frequency errors outside this volume (see fig. 2). The cutoff N for the series was determined by the regularization scheme described above, and in this case was $N = 5$ (the maximum allowed) for each of the three partial fields.

The result for the reconstruction of the intensity vector at 732 Hz in the described volume for the first partial field is shown in fig. 10. Two views of the volumetric field are shown and the square grey patch is a cartoon showing the location of the fuselage window (recall that the point source was at the center of this window). The dominant reference x_m (using Eq. (18)) turned out not surprisingly to be the drive voltage for the loudspeaker. Clearly the location of the real source is uncovered by the intensity display, hopefully a convincing demonstration of the success of the approach. The reference x_n related to the second partial field was the accelerometer shown in fig. 9 (number 17) located on the resonant panel below the

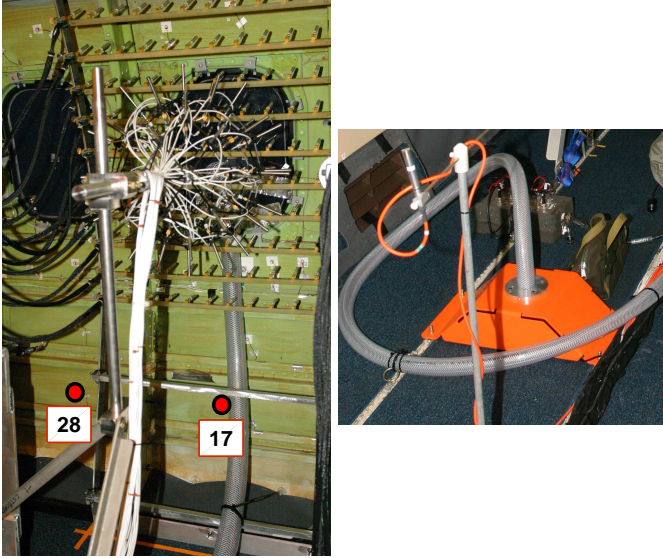


FIG. 9. Acoustic point source installed inside the 757 cabin. The end of the vertical tube simulating a point source radiates sound near the center of the window (somewhat obscured by the conformal array). The tube is excited by a loudspeaker resting on the floor of the cabin that is coupled to the other end of the tube (shown on right). Red dots mark the position of two reference accelerometers.

window. This result is shown in fig. 11. Although the exact location of the resonant panel source (located 0.9m from the sphere center) is not clearly identifiable, the flow of the intensity clearly indicates a source below the window. Interestingly, the intensity flow diffracts along a path that is tangential to the fuselage surface. (Note we will show below that the same diffraction arises when the point source is turned off). Finally, the third partial field is shown in fig. 12, which is correlated to accelerometer number 28 located at the center of the panel directly to the left of the resonant panel described above. This panel, identical in shape, was also resonant at 732 Hz, and the results for the volumetric intensity for this partial field is shown in fig. 12. Note that the intensity appears to now come from the bottom left, that is, from the direction of the resonant panel, although possibly interrupted by the king frame that is located in between. The total amount of signal “energy” represented by the first three partial fields, given by Eq. (24) with $M = 3$, was 84% indicating that only 16% of the total signal energy was unaccounted for.

1. Discussion

The reference (electrical drive) for the first partial field is incoherent ($\gamma^2 \approx .003$) to each of the two accelerometers (numbered 17 and 26 in fig. 9) and the Cholesky method works well to provide a unique decomposition

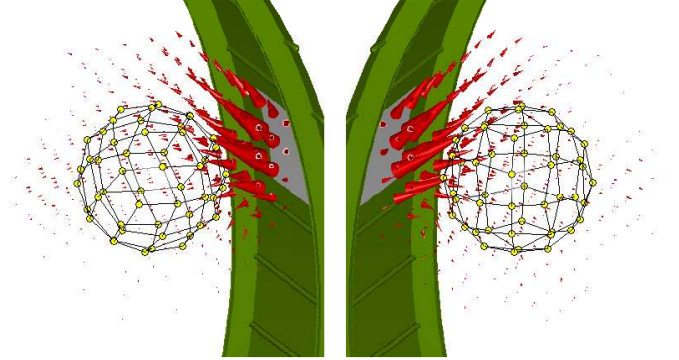


FIG. 10. Point source on: 732 Hz 1st partial field. The first partial field contained 59% of the total signal energy according to Eq. (23). The total acoustic energy in vector field shown was $9.91\mu\text{J}$.

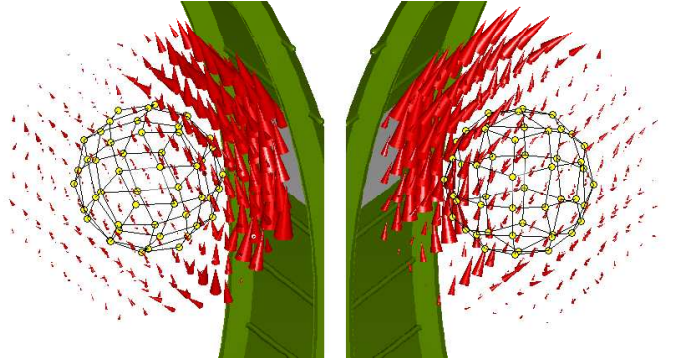


FIG. 11. Point source on: 732 Hz 2nd partial field. The second partial field contained 18% of the total signal energy according to Eq. (23). The total acoustic energy in vector field shown was $2.21\mu\text{J}$.

and a separation of the incoherent fields. As long as the references are incoherent, the extraction is straightforward and successful as previous research has shown.^{14–16} The difficulty here comes with a set of accelerometer references that respond to flow noise that in itself has some spatial coherence, and thus the individual panels on the fuselage section are *somewhat* coherent to one another. After the point source is removed, there are no

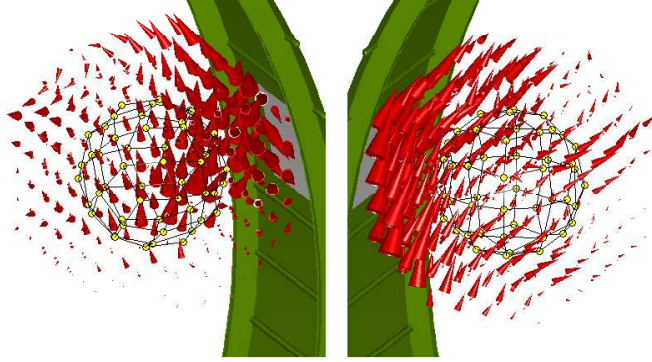


FIG. 12. Point source on: 732 Hz 2nd partial field. The second partial field contained 6% of the total signal energy. The total acoustic energy in vector field shown was $0.70\mu\text{J}$.

incoherent sources left, since the various aircraft panels are weakly coupled. However, the Cholesky method forces incoherence (albeit artificial) here. That is, in view of the fact that the Cholesky method is identical to the signal conditioning approach²⁰ we can understand the Cholesky method as one that extracts the uncorrelated components of the reference signals in successive partial fields. In our case one can view the 3rd partial field as an extraction out of the 1st two partial fields by creating a signal that is orthogonal or incoherent to them and in the process of doing this creates a volumetric intensity field that appears to come from the panel to the left. The raw accelerometer signals themselves are correlated to each other, in our case with a coherence of 0.33. This orthogonalization is somewhat artificial as it depends on the order of the references chosen before the Cholesky decomposition is carried out. We have chosen to order based on descending average coherences using Eq. (18) but other ordering methods may be used. In other words, when correlated references exist in the reference set, one is not guaranteed a one to one relationship between the partial field vector intensity and the orthogonalized reference. The intensity field may appear to come from one of the other closely correlated references, instead. However, this is not the case if the references are uncorrelated and the order of the references will not change the results. Although not discussed in this paper, partial fields based on the SVD decomposition instead of Cholesky do not suffer from this ordering problem. We will present results on this in a later paper.

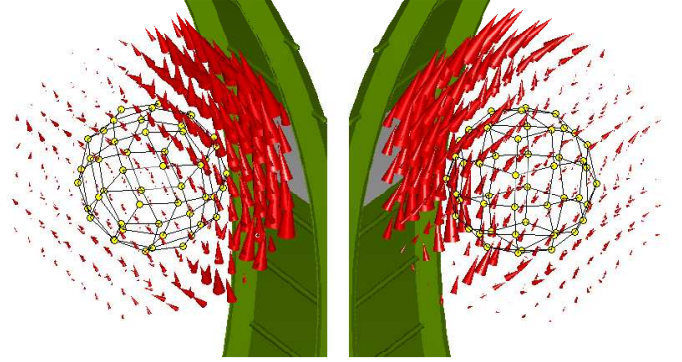


FIG. 13. Point source is turned off. Result for the first partial field at 732 Hz. This field contained 45% of the total signal energy. The total energy in vector field shown was $2.53\mu\text{J}$.

B. Repeat experiment with point source turned off

The experiment described in Sec. VI.A was repeated about 20 minutes later with the acoustic point source turned off, and the results were computed in the same frequency bin for comparison. An effort was made to keep the aircraft speed and altitude unchanged. The resulting first partial field is shown in fig. 13 and the maximum coherence to the microphones determined by Eq. (18) was accelerometer number 17, the same reference found for the second partial field when the source was on, in the previous experiment. A close comparison to fig. 11 reveals an important result. The flow fields are identical. This gives credibility to the conclusion that the vector field for the point source was accurately separated from the other incoherent sources in the previous experiment. Furthermore, this agreement shows the robustness of the approach.

Finally we present the results for the second partial field when the source is off, shown in the next figure. The reference associated with the field was accelerometer number 28, and a direct comparison with the previous result fig. 11, also correlated to the same accelerometer, can be made. Again a remarkable result occurs - the intensity vector fields are nearly identical, again showing an intensity field that appears to emanate from an area near the reference accelerometer (see fig. 9) on the panel to the left. Again the robustness of the field extraction approach is demonstrated, even in the face of the coherence in the vibration between the two panels involved.

We have shown only two of the 32 partial fields computed. The remaining partial fields represent a small fraction of the total signal energy with less than 2.5% each, and appear to be nearly buried in the noise.

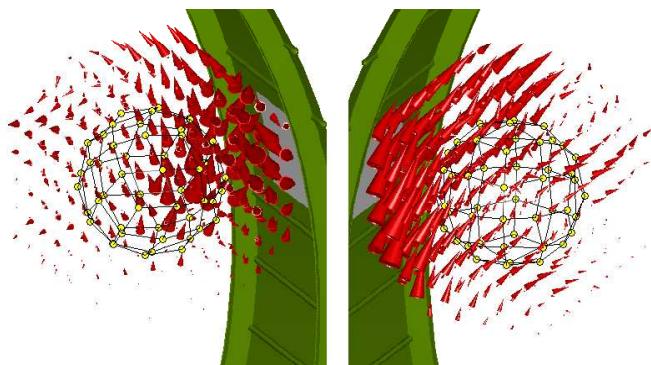


FIG. 14. Point source is turned off. Result for the second partial field at 732 Hz. This field contained 18% of the total signal energy. The total energy in vector field shown was $0.81\mu\text{J}$

VII. CONCLUSIONS

The work presented here is a small fraction of the theory and development of the VAIP, and future papers will discuss more details such as SVD partial field decomposition results, use of self referencing to a set of microphones in the array without external references and 1/3 octave band results as well as new generation designs of the array. The aim in the design and the algorithm behind the intensity computations is for real time display, so that the system would provide nearly instantaneous results when used with a laptop in the field. With this the VAIP can scan a large space making volumetric reconstructions on the fly. We believe that this will provide an invaluable tool for source identification both in air and underwater.

Acknowledgments

Work supported by the Office of Naval Research. Experimental work and data analysis was supported by NASA Langley and The Boeing Company provided critical experiment support.

- ¹ T. J. Schultz, "Acoustic wattmeter", *J. Acoust. Soc. Am.* **28**, 693–699 (1956).
- ² F. J. Fahy, *Sound Intensity* (Elsevier Applied Science, London) (1989).
- ³ S. Nagata, K. Furihata, T. Wada, K. Asano, and T. Yanagisawa, "A three-dimensional sound intensity measurement system for sound source identification and sound power determination by In models", *J. Acoust. Soc. Am.* **118**, 3691–3705 (2005).

- ⁴ R. D. Marciniak, "A nearfield, underwater measurement system", *J. Acoust. Soc. Am.* **66**, 955–964 (1979).
- ⁵ G. Weinreich and E. B. Arnold, "Method for measuring acoustic radiation fields", *J. Acoust. Soc. Am.* **68**, 404–411 (1980).
- ⁶ M. Park and B. Rafaely, "Sound-field analysis by plane-wave decomposition using spherical microphone array", *J. Acoust. Soc. Am.* **118**, 3094–3103 (2005).
- ⁷ J. E. Hansen, ed., *Spherical near-field antenna measurements* (Peter Peregrinus Ltd. for Institution of Electrical Engineers, London, UK) (1988).
- ⁸ R. C. Wittmann, "Spherical wave operators and the translation formulas", *IEEE Trans. Antennas Propagat.* **36**, 1078–1087 (1988).
- ⁹ E. G. Williams, *Fourier Acoustics: Sound Radiation and Nearfield Acoustical Holography* (Academic Press, London, UK) (1999).
- ¹⁰ V. I. Lebedev, "Values of the nodes and weights of ninth to seventeenth order gauss-markov quadrature formulae invariant under the octahedron group with inversion", *Sh. vychisl. Mat. mat. Fiz.* **15**(1), 48–54 (1975).
- ¹¹ V. I. Lebedev, "Quadratures on a sphere", *USSR Comput. Math. and Math. Phys.* **16**(2), 10–24 (1976).
- ¹² E. G. Williams, "Regularization methods for near-field acoustical holography", *J. Acoust. Soc. Am.* **110**, 1976–1988 (2001).
- ¹³ P. C. Hansen, *Rank-Deficient and Discrete Ill-Posed Problems* (Siam, Philadelphia, PA) (1998).
- ¹⁴ J. Hald, "STSF - a unique technique for scan-based nearfield acoustical holography without restriction on coherence", Technical Report, B&K Technical Review, No. 1 (1989).
- ¹⁵ D. L. Hallman and J. S. Bolton, "Multi-reference nearfield acoustical holography", in *Proceedings Inter-noise '92*, 1165–1170 (Toronto, Canada) (1992).
- ¹⁶ D. L. Hallman and J. S. Bolton, "A comparison of multi-reference nearfield acoustical holography procedures", in *Proceedings Noise-Con '94*, 929–934 (Ft. Lauderdale, Florida) (1994).
- ¹⁷ H.-S. Kwon and J. S. Bolton, "Partial field decomposition in nearfield acoustical holography by the use of singular value decomposition and partial coherence procedures", in *Proceedings Noise-Con '98*, 649–654 (1998).
- ¹⁸ H.-S. Kwon, Y.-J. Kim, and J. S. Bolton, "Compensation for source nonstationarity in multireference, scan-based near-field acoustical holography", *J. Acoust. Soc. Am.* **113**, 360–368 (2003).
- ¹⁹ K.-U. Nam and Y.-H. Kim, "A partial field decomposition algorithm and its examples for near-field acoustic holography", *J. Acoust. Soc. Am.* **116**, 172–185 (2004).
- ²⁰ J. S. Bendat and A. G. Piersol, *Random Data Analysis and Measurement Procedures*, third edition (John Wiley & Sons, New York, NY) (2000).
- ²¹ M. A. Tomlinson, "Partial source discrimination in near field acoustic holography", *Applied Acoustics* **57**, 243–261 (1999).
- ²² J. Klos and et. al., "Comparison of different measurement technologies of the in-flight assessment of radiated acoustic intensity", in *Proceedings of Noise-Con 2005* (Minneapolis, Minnesota) (2005).